Array Analysis of Seismo-Volcanic Activity with Distributed Acoustic Sensing

Francesco Biagioli, Jean-Philippe Métaxian, Eléonore Stutzmann, Maurizio Ripepe, Pascal Bernard, Alister Trabattoni, Roberto Longo, Marie-Paule Bouin

▶ **To cite this version:**

Francesco Biagioli, Jean-Philippe Métaxian, Eléonore Stutzmann, Maurizio Ripepe, Pascal Bernard, et al.. Array Analysis of Seismo-Volcanic Activity with Distributed Acoustic Sensing. Geophysical Journal International, In press, ⟨10.1093/gji/ggad427⟩. ⟨hal-04300894⟩

HAL Id: hal-04300894

https://hal.science/hal-04300894v1

Submitted on 22 Nov 2023

HAL is a multi-disciplinary open access archive for the deposit and dissemination of scientific research documents, whether they are published or not. The documents may come from teaching and research institutions in France or abroad, or from public or private research centers.

L'archive ouverte pluridisciplinaire **HAL**, est destinée au dépôt et à la diffusion de documents scientifiques de niveau recherche, publiés ou non, émanant des établissements d'enseignement et de recherche français ou étrangers, des laboratoires publics ou privés.

HAL Authorization

Geophys. J. Int. () , 1–**??**

Array Analysis of Seismo-Volcanic Activity with Distributed Acoustic Sensing

Francesco Biagioli,[1,2⋆], Jean-Philippe Métaxian[1], Eléonore Stutzmann[1], Maurizio Ripepe[2], Pascal Bernard[1], Alister Trabattoni[3],Roberto Longo[4], Marie-Paule Bouin[1]

[1]*Institut de Physique du Globe de Paris, Université Sorbonne-Paris-Cité, CNRS, France, e-mail: biagioli@ipgp.fr,*
[2]*Department of Earth Sciences, University of Florence, Firenze, Italy,*
[3]*Université Côte d'Azur, IRD, CNRS, Observatoire de la Côte d'Azur, Géoazur, Valbonne, France,*
[4]*Groupe Signal Image et Instrumentation (GSII), École Supérieure d'Électronique de l'Ouest (ESEO), Angers, France.*

24 August 2023

SUMMARY
Continuous seismic monitoring of volcanoes is challenging due to harsh environments and associated hazards. However, the investigation of volcanic phenomena is essential for eruption forecasting. In seismo-volcanic applications, Distributed Acoustic Sensing (DAS) offers new possibilities for long-duration surveys. We analyse DAS strain rate signals generated by volcanic explosions and tremor at Stromboli volcano (Italy) recorded along 1 km of dedicated fibre-optic cable. We validate DAS recordings with co-located nodal seismometers. Converting node measurements to strain rate, we observe a perfect match in phase between DAS and node waveforms. However, DAS amplitudes appear to be around 2.7 times smaller than those of node records, which we explain as due to the inefficient ground-to-fibre strain transfer in the loose cable. We invert time delays between strain rate waveforms and confirm that the DAS enables us to retrieve a dominant and persistent seismic source in the proximity of active craters. This stable source location is confirmed by node array analyses. Despite an observed high noise level of strain rate signals outside a range of 2–15 Hz, our results demonstrate the potential of this new technology in monitoring volcanic areas.

Key words: Volcano seismology; Volcano monitoring; Time-series analysis; Explosive volcanism.

1 INTRODUCTION

Volcano seismology is essential to investigate the various and complex signals generated by volcanic phenomena, as well as for eruption forecasting and monitoring (Chouet & Matoza, 2013; McNutt & Roman, 2015). Seismic arrays have been proven effective in detecting and locating even faint seismo-volcanic signals (e.g., Inza et al. 2011; La Rocca et al. 2004; Hansen & Schmandt 2015; Glasgow et al. 2018). Dense arrays also improve observations of spatial and temporal changes within the subsurface (e.g., Takano et al. 2020; Bruno et al. 2017). However, volcanic areas are remote and harsh environments presenting high hazard levels. Installing and maintaining seismic arrays in these contexts poses significant challenges. After an initial use in the oil and gas industry (Hartog, 2017), Distributed Acoustic Sensing (DAS) is nowadays widespread in other fields of geophysical application, such as earthquake seismology (Wang et al., 2018; Williams et al., 2019; Jousset et al., 2018; Sladen et al., 2019) and near-surface seismic characterisation and monitoring (Spica et al., 2020; Fang et al., 2020; Dou et al., 2017; Daley et al., 2013; Ajo-Franklin et al., 2019).

In seismo-volcanic contexts, DAS offers new possibilities for long-duration surveys at high temporal (up to kHz) and spatial (to the metre scale) resolutions with reduced risks and costs. DAS measures dynamic longitudinal strain via optical interferometry of the Rayleigh backscattered light of emitted coherent laser pulses, whose signature changes when the cable is lengthwise deformed by propagating seismic waves (Hartog, 2017; Lu et al., 2019; Lindsey et al., 2020). Via the DAS technique, a single interrogation unit can simultaneously probe tens of kilometers of a fibre-optic cable, mimicking a large, meter-scale array of synchronized single-component sensors (Lindsey et al., 2017; Hartog, 2017). DAS measurements can be performed remotely at a fibre end, hosting the interrogation unit in a safe location (Nishimura et al., 2021; Jousset

⋆ Corresponding author: Francesco Biagioli, biagioli@ipgp.fr

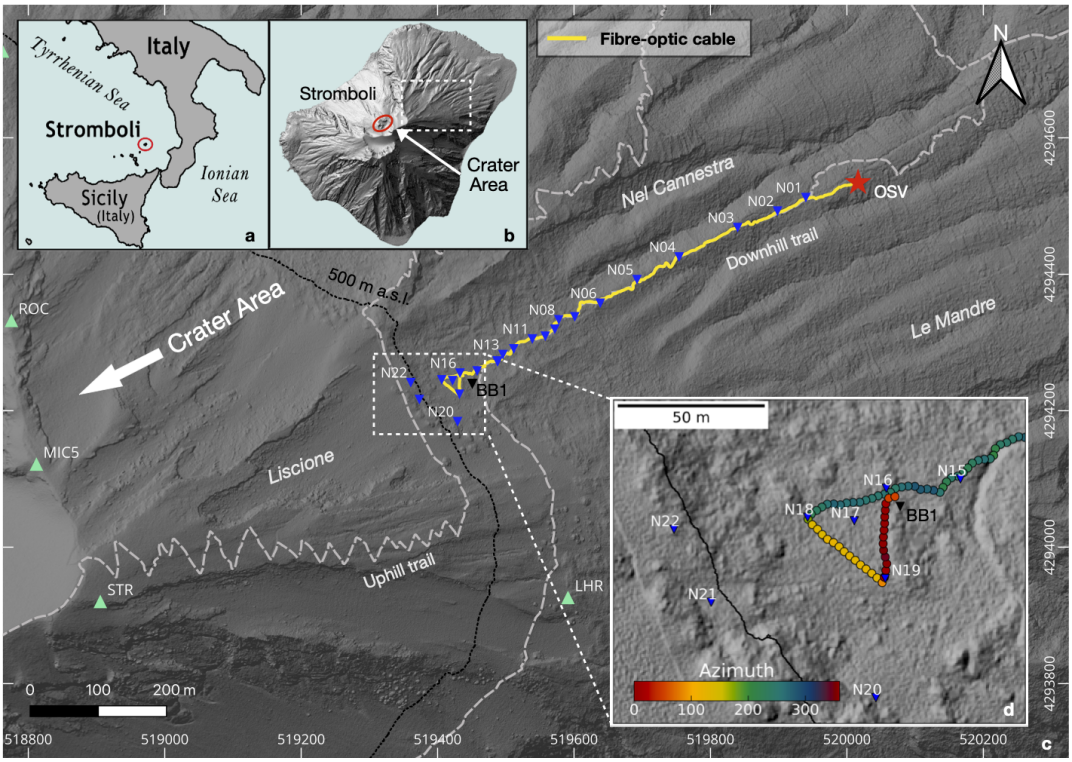

Figure 1. High-resolution digital elevation model (DEM) of Stromboli Northeast flank. The fibre-optic cable (yellow line), the 22 SmartSolo nodes numbered from N1 to N22 (blue triangles), the broadband station BB1 (black triangle) are displayed. Some node names are omitted for visual reasons, however they are named from N1 to N22 in a progressive manner starting from the Geophysical Observatory (OSV, red star). Green triangles mark the location of the seismic (ROC, STR), infrasonic (MIC5), and tiltmeter (LHR) stations of the Laboratory of Experimental Geophysics (LGS, University of Florence). (Bottom right) Magnified view of the triangle-shaped DAS and seismic arrays, with DAS channels colored according to their azimuth with respect to the North. The DAS interrogator was hosted inside the OSV. The DEM is computed from images taken in 2014 and courtesy of Italian Civil Protection.

et al., 2022). The optical cable can be buried at a sufficient depth to mitigate the risk associated with eruptive events.

Previous DAS experiments on volcanoes exhibited promising results. Nishimura et al. (2021) located the hypocenters of shallow volcanic earthquakes and estimated site effects at Azuma volcano, Japan. Klaasen et al. (2021) revealed the presence of a high and low-magnitude seismicity at Mount Meager, British Columbia. At mount Etna, Italy, Currenti et al. (2021) efficiently compared DAS strain measurements with broadband inertial-seismometers, while Jousset et al. (2022) recorded the seismo-acoustic waves associated with small-scale volcanic events linked to fluid migration. This latter study also imaged shallow structural heterogeneities. Currenti et al. (2023) detected and analysed Very Long Period (0.01-0.2 Hz) seismic signals at Volcano island, Italy, during a volcanic unrest phase.

Stromboli volcano exhibits a persistent ordinary activity (Rosi et al., 2000) accompanied by a high explosion rate ($\sim$13 events/hour; Ripepe et al., 2008), and emits signals in a wide range of frequencies (10^{-2} – 10 Hz; Neuberg et al. 1994; Chouet et al. 2003, 1997). These characteristics make it one ideal test bench for DAS applications at volcanoes. The origin of the explosions is generally attributed to the nucleation, rise and final burst of gas slugs in the conduit (Blackburn et al., 1976). A continuous and less energetic volcanic tremor is also observed in the seismic records, with frequencies mainly between 1–5 Hz (Ripepe et al., 1996; Langer & Falsaperla, 1996; Nappi, 1976; Wassermann, 1997). Tremor signals at Stromboli are inferred to be linked with the coalescence of small ($<$0.5 m) gas bubbles in the conduit bursting every $\sim$ 1–2 s (Ripepe & Gordeev, 1999).

However, this ordinary activity can be occasionally interrupted (or accompanied) by lava flows and violent explosions, the so-called Strombolian paroxysms (Métrich et al., 2021; Ripepe et al., 2021b). Those events represents a major threat for both inhabitants and tourists due to the wide areal coverage of the volcanic ballistic projectiles and the potential formation of pyroclastic flows (Rosi et al., 2013).

To address these challenges, we aim to demonstrate that the strain rate recorded by DAS at Stromboli can be used to monitor volcanic explosions and tremor. Seismo-volcanic signals as those observed at Stromboli are spindle-shaped and characterised by emergent onsets without marked S-wave arrivals (Métaxian et al., 2002; La Rocca et al., 2004; Wassermann, 2012). Furthermore, volcanic tremor is a continuous signal lacking clear body-wave phases (Chouet, 1996). It is difficult to locate these signals with classical methods of hypocenter determination (Métaxian et al., 2002; Wassermann, 2012; Inza et al., 2014).

To circumvent this difficulty, we can use array processing methods, such as delay-and-sum beamforming (Capon et al., 1967; Schweitzer et al., 2012) or Multiple Signal Classification (MUSIC; Schmidt, 1986), commonly used in volcanic areas (Chouet, 1996; Wassermann, 1997; Inza et al., 2011, 2014; Leva et al., 2022). These methods provide insights into seismic wave propagation direction and apparent velocity. Several studies exhibit results of these methodologies applied to DAS arrays with linear to more complex geometries (Lindsey et al., 2017, 2019; Fang et al.,

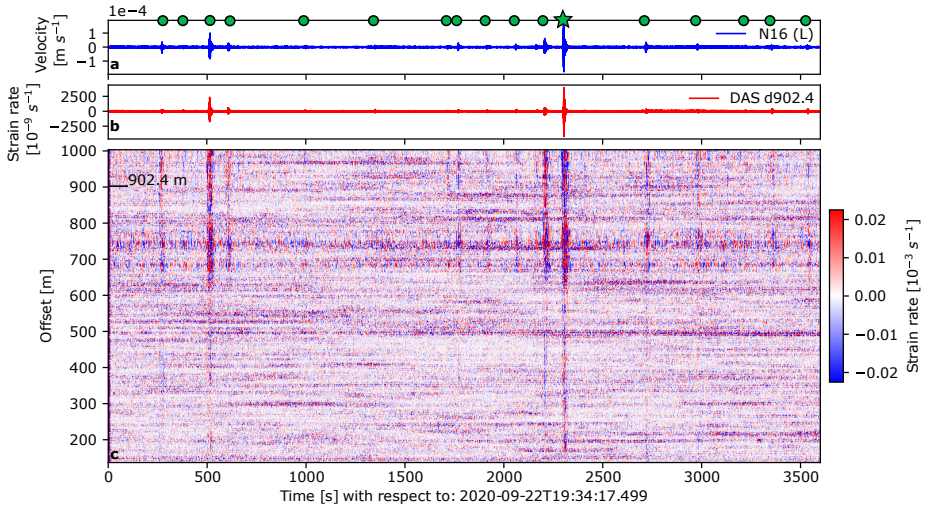

Figure 2. (a) Velocity recorded by the L component of node N16 on 09/22/2020 from 19:34 to 20:34. (blue). (b) Strain rate at co-located DAS channel d902.4 for the same time interval (red). Green circles in (a) mark the explosive events detected with a recursive STA/LTA algorithm (Beyreuther et al., 2010). The green star marks the largest event. (c) Strain rate record at each of the 362 DAS channels ordered according to their offset from the DAS interrogator. The black horizontal segment marks the DAS channel d902.4. Data are filtered between 1–10 Hz in this figure.

2020; Klaasen et al., 2021; van den Ende & Ampuero, 2021; Nayak et al., 2021; Jousset et al., 2022). In these studies, either single events or events selected by signal detection methods are analysed. In volcanic environments, Klaasen et al. (2021) applied beamforming analysis to high frequency earthquakes most likely related to geothermal fluid movements, while Jousset et al. (2022) located the source of volcanic explosions. Yet, to our knowledge, there has been no reports of employing these or other array techniques to analyse continuous strain rate signals consisting of volcanic tremor together with explosions.

This manuscript is organized as follows. First, we provide a comprehensive account of the fieldwork and the experimental setup (Section 2). We then present and compare data recorded with the DAS and with a co-located seismic array (Sections 3 and 4). Afterwards, we estimate the slowness vector with seismic velocity and strain rate records using array processing techniques (Section 5). Finally, we discuss the results and their significance regarding the use of DAS for volcanic monitoring (Sections 6 and 7).

2 FIELD EXPERIMENT AND DATA

2.1 Description of the field-work

In September 2020, we deployed 1 km of dedicated fibre-optic cable at Stromboli volcano (Fig. 1). The cable is composed of a polyethylene jacket which encloses a loose kevlar layer surrounding 8 tight-buffered optical fibres (see Supplementary Note A in the Supplementary Information). We started from the Geophysical Observatory of the University of Florence, located at an altitude of 200 m a.s.l., and we continued along the path towards the summit. We faced several challenges including the steep slope, the high density of the vegetation below 400 m a.s.l., and the ashy nature of the soil. The trench was dug by hand by local workers, while the scientific team buried the cable trying to ensure the best possible coupling with the ground. This was sometimes complicated in areas of steep drop or in curves because of the nature of the soil. The cable was buried about 30 cm deep over a length of 870 m. First, we followed a path oriented towards the craters. Then, we implemented a triangular array with sides measuring 30 meters at the path's endpoint (Fig. 1d). This specific design allowed us to measure strain rate in directions other than the main cable path and test array processing techniques using DAS data. In this higher area, the fibre was installed under a steep ($\sim 25°$) but relatively flat slope characterised by poor vegetation at an altitude of ~ 450 m a.s.l.

The DAS interrogator (Febus A1-R) was hosted inside the Geophysical Observatory. We carried out DAS measurements for 1 week, from September 15 to 23, 2020, with continuous recording sessions of 7 to 8 hours per day. We recorded strain rate data with a sampling frequency of 2 kHz, a spatial interval of 2.4 m and a gauge length of 5 m leading to a number of 362 useful channels.

22 nodes SmartSolo IGU-16HR 3-component (3C) nodes (named from N1 to N22 progressively from the Geophysical Observatory) with a corner frequency of 5 Hz and a sampling rate of 250 Hz were installed along the fibre path (Fig. 1, blue triangles) during the second half of the experiment. A Guralp digitizer equipped with a CMG-40T 30 sec seismometer and an infrasound sensor (station BB1) was placed in the upper part of the path, close to the lower corner of the triangle (Fig. 1, black triangle). The inertial sensor distribution along the path of the fibre optic cable was designed such that we could compare records made with the different technologies. DAS, nodes, and the broadband seismometer recorded simultaneously between 20 and 23 September 2020.

2.2 Pre-processing

To geolocalise each DAS channel we carried out a series of 56 taps along the fibre. By searching for the earliest arrival times, we obtained the relative positions along the cable of a subset of channels as well as their GPS positions. The latter were measured by a kinematic GPS survey. For this purpose, we used 2 Leica GR25 receivers. One of these was installed in a fixed position and in continuous recording at the Geophysical Observatory while we made a pathway with the second. The channels are linearly interpolated along the fibre GPS layout in between the positions of the 56 taps.

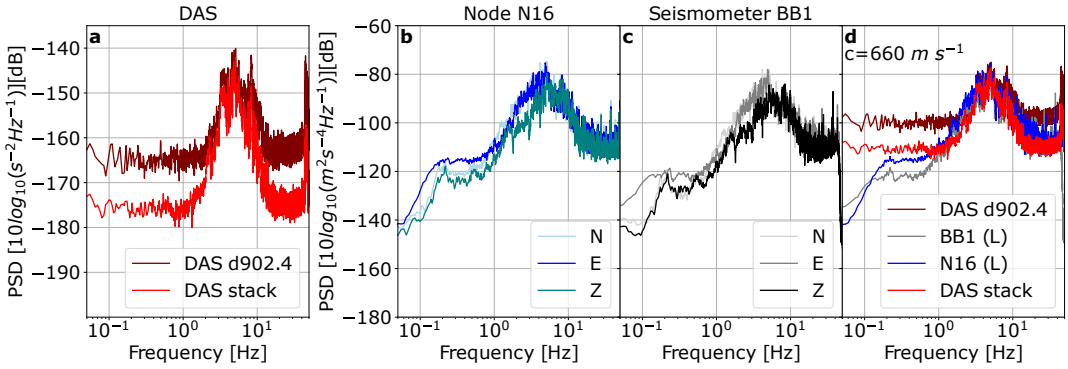

Figure 3. PSDs computed during the hour-long time series (09/22/2020 19:34–20:34 UTC) for different unfiltered records: (a) PSD of DAS channel d902.4 (brown) and stack of the PSDs calculated for the channels d892.8-912.0 (red), in strain rate. (b) and (c) PSDs of the 3 components of co-located node N16 and broadband seismometer BB1, in acceleration. (d) PSDs of the DAS channel d902.4 and the DAS d892.8–912.0 channel stack converted to acceleration using Eq. (1), and the L components of N16 and BB1, in acceleration.

Strain rate data are decimated to 200 Hz. Seismometers are corrected for their instrumental response.

3 DATA

During the experiment, the volcano showed a typical Strombolian regime, characterised by a number of ordinary explosive events around 14 events/hour emitting acoustic pressures lower than 0.5 bar. A persistent volcanic tremor of amplitude between 1–3 μm/s was also present. We analyse the entire dataset acquired during the experiment. In this work, we show the results for one hour of raw measurements between 19:34–20:34 UTC on 09/22/2020. Due to the level of volcanic activity, this period of time includes 17 explosive events of varying intensity. A persistent volcanic tremor is also present as a background signal throughout the entire hour.

Fig. 2 exhibits an example of both strain rate and seismic velocity recorded during one hour and filtered between 1–10 Hz, that is in the spectral band of explosion-quakes (1-10 Hz) and volcanic tremor (1-5 Hz) at Stromboli (Ripepe et al., 1996; Langer & Falsaperla, 1996; Chouet et al., 1997). Fig. 2a shows the seismic velocity of the so-called L component of node N16 along the direction of the co-located fibre-optic cable obtained by rotation (azimuth:250°and tilt:22°). Fig. 2b shows the strain rate of co-located DAS channel d902.4. We observe the same events in both strain rate and velocity time series.

We then compare power spectral densities (PSDs) for one hour (09/22/2020 19:34–20:34 UTC) of unfiltered signals recorded by DAS, nodes and the broadband seismometer. Fig. 3a shows the strain rate PSD of DAS channel d902.4. For comparison, we also plot the PSD stacked for channels d892.8–912.0 (i.e., in a 20 m window centred on channel d902.4). Fig. 3b,c show the seismic acceleration PSDs of the Z, N, and E components of co-located N16 node and BB1 broadband seismometer, respectively. In Fig. 3d we compare the seismic acceleration PSDs of the L component of N16 and BB1 with the seismic acceleration obtained from the strain rate used in Fig. 3a using the following relation (e.g., Aki & Richards 2002, Daley et al. 2016, Wang et al. 2018, Jousset et al. 2018):

$$\dot{\varepsilon} = \pm \ddot{u}/c, \qquad (1)$$

where $\dot{\varepsilon}$ is the DAS strain rate, $\ddot{u}$ is the seismic acceleration and

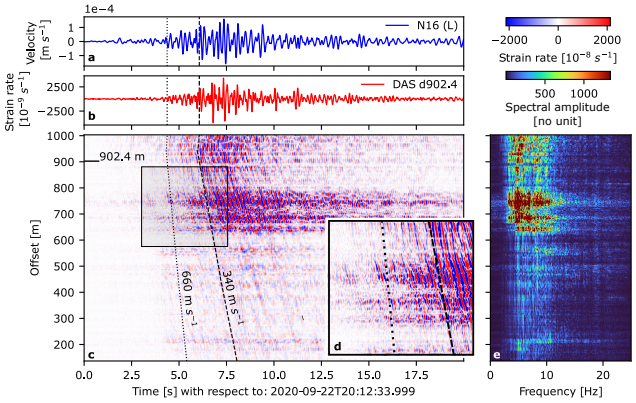

Figure 4. (a) velocity measurement of the L component of node N16 (blue) during an explosive event occurred at 20:14:30 UTC on 2020/09/22 (green star in Fig. 2). (b) Strain rate of the same event at co-located DAS channel d902.4 (red). (c) Strain rate record at each of the 362 DAS channels ordered according to their offset from the DAS interrogator. Black horizontal line in (c) marks the location of DAS channel d902.4 along the cable. (d) Zoom-in of the frame in (c). Dashed lines in (a–d) mark the theoretical arrival times at the several sensors of waves with velocities of 660 and 340 m/s starting from the onset of the acoustic wave at the source as recorded by the MIC5 infrasonic station (Fig. 1). (e) Frequency domain representation of the strain rate record below 25 Hz along the fibre for the 20 s of the explosion.

c is the apparent phase velocity along the cable direction. We rescale the strain-rate PSDs by considering an apparent velocity of 660 m/s and an amplitude correction factor of 2.7. This apparent phase velocity corresponds to the dominant signals and is determined in Section 5.4. The amplitude correction factor is obtained after a proper calibration of DAS strain rate measurements in Section 4.

After correcting the amplitudes by the factor 2.7 we observe a good match between the acceleration PSDs derived from DAS and recorded by the L components of N16 and BB1 in the frequency range 2–10 Hz (Fig. 3d). Outside this frequency band, the DAS acceleration PSD corresponding to the single channel d902.4 exhibits higher (∼15 dB) values of noise levels (Fig. 3a,d). As pointed out by e.g. Hudson et al. (2021), stacking the PSDs computed for multiple DAS channels results in improved signal-to-noise ratios. In our case (Fig. 3a,d), we obtain lower noise levels below 3 Hz and above

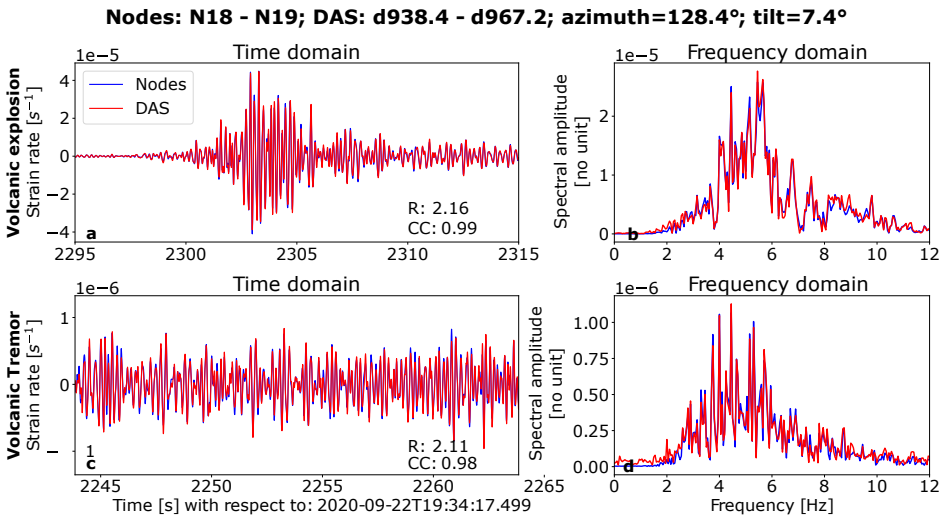

Figure 5. Comparison between the strain rate traces recorded by DAS (red) and obtained from nodes (blue) using Eq. (2) across the segment N18–19 (DAS channels d938.4–d967.2) for one explosive event (top row) and 20 s of volcanic tremor (bottom row), in both time (left column) and frequency (right column) domains. The ratios (R) between the RMS amplitudes of node and DAS traces, and the maximum cross-correlation coefficients (CC) between the two waveforms are shown in the bottom right of (a) and (c). To enhance clarity, we rescale DAS strain rate traces by multiplying them with the ratio R.

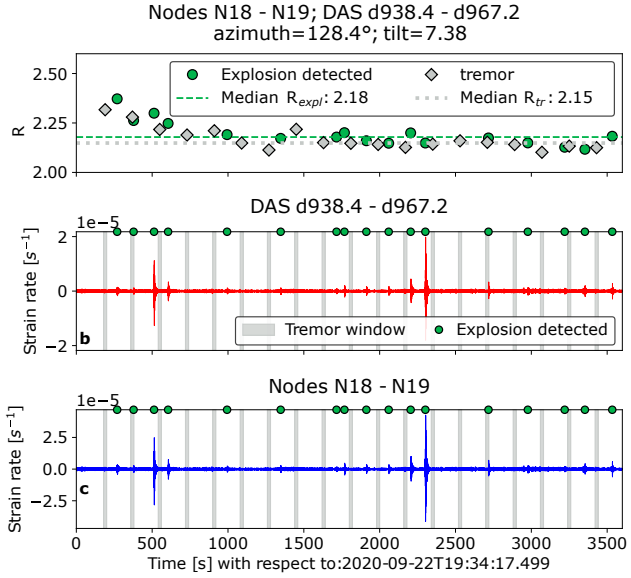

Figure 6. (a) Ratios (R) between the RMS amplitudes of strain rate obtained from nodes and DAS along segment N18-19 are calculated for various time windows throughout the entire hour shown in Fig. 2. This includes 17 volcanic explosions detected using an STA/LTA algorithm (green circles) and 20 windows containing volcanic tremor signals each with a length of 20 seconds (gray diamonds). The green dashed line in (a) represents the median value of the ratios R_{expl} calculated from explosion signals. The gray dotted line in (a) represents the median value of the ratios R_{tr} calculated from tremor signals. (b) DAS cumulative strain rate trace along the segment. (c) Node-derived strain rate trace along the segment. In (a) and (b), green circles indicate the detected explosions and gray vertical bars represent the 20-second long tremor windows used to compute R in (a).

10 Hz than in the case of an individual DAS channel. However, the DAS noise level is still too high to observe the 0.1–0.14 Hz spectral peak corresponding to secondary microseisms (e.g., Stutzmann et al. 2009). It is instead visible on acceleration PSDs of the N and Z components of the seismometers (Fig. 3b,c). We note that this spectral peak is also scarcely visible in the PSDs of the L components for BB1 and N16 (Fig. 3d).

The time-domain signal from DAS channel d902.4 converted into acceleration using Eq. (1) bears good resemblance to those recorded by the L components of N16 and BB1 (Fig. 3d). The maximum cross-correlation coefficients between the DAS-derived acceleration and N16/BB1 are 0.6 for the entire hour in Fig. 2 and 0.7 when specifically analysing the explosion at 20:14:37 UTC on 09/22/2020 (marked by a green star in Fig. 2).

Fig. 4a,b show the signals generated by this explosion recorded by one node and the co-located DAS channel. The dominant frequencies are mainly between 2–15 Hz (Fig. 4e). Fig. 4c displays the strain rate recorded by the entire DAS array. The slope of the wavefronts gives the apparent velocity along the fibre. For comparison, we compute the theoretical arrival times for waves traveling from the craters to each sensor starting from the onset of the infrasonic pressure wave (20:14:37 UTC) as recorded by the MIC5 acoustic station (Fig. 1). We do not take into account the topography and choose velocities of 660 m/s (corresponding to the dominant signals obtained from the array analysis in Section 5.4) and 340 m/s (i.e., the acoustic wave velocity). We observe that the ground-coupled (Braun & Ripepe, 1993) infrasonic pressure wave (340 m/s) is visible on both DAS and seismic data at the time marked by the dashed line in Fig. 4a-d. Although it is not the most energetic phase observed, the infrasonic wave propagates all along the cable (Fig. 4c,d).

Furthermore, we observe in Fig. 4c an area between DAS channels d662.4–d751.2 (zoomed in Fig. 4d) where the wavefronts exhibit smaller slopes comparable with apparent velocities lower than the sound speed. The area also displays larger strain rate signals, reaching up to ten times the amplitudes found in other fibre sections. Moreover, this portion of the cable deployment correlates quite precisely with a change in topography along the slope. This change can be observed in Fig. 1 close to node N06 (at approximately 360 m a.s.l.). Northeast (and at lower altitudes) of node N06, lava flows are visible. To the southwest (and at higher altitudes) the lava flows disappear where the topography becomes smoother due

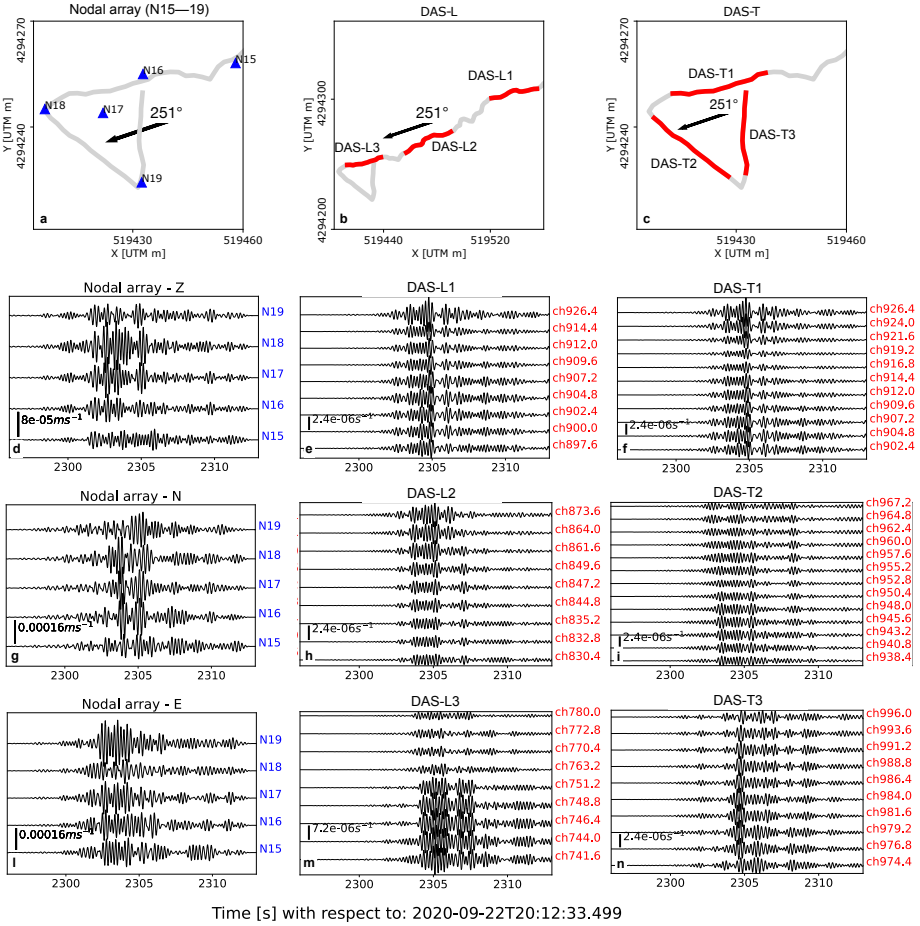

Figure 7. Geometry of the nodal array N15–19 (a) and of the DAS-L (b) and DAS-T (c) arrays. The black arrow in (a-c) indicates the back-azimuth (251°) of the central part of the active craters with respect to the centroid of each array. (d-n) show the traces for an explosive event (same as in Fig. 4). (d, g, l) show the 3 components of the 5 nodes. (e, h, m) show the 10 DAS channels along the 3 segments of the DAS-L array. (f, i, n) show the 10 DAS channels along the 3 segments of the DAS-T array. Traces are band-pass filtered in the 3–5 Hz frequency range.

to ash coverage (see Fig. S1 in Supplementary Information). This is discussed in more detail in Section 6.

4 DAS DATA CALIBRATION

Prior to any further analysis, we calibrate and evaluate the quality of DAS recordings by comparing it with the strain rate retrieved from co-located nodes. The average strain rate along a linear segment of length nL_G (where n is the number of gauge lengths L_G contained in the segment) can both be estimated by stacking the strain rate $\dot{\varepsilon}$ recorded by DAS or by differentiating the seismic velocities $\dot{u}$ in the cable direction at the two endpoints of the segment (van den Ende & Ampuero, 2021). This translates in the following finite-difference relationship (Wang et al., 2018):

$$\dot{\varepsilon}|_{x=-(n-1)L_G/2} + \cdots + \dot{\varepsilon}|_{x=0} + \cdots + \dot{\varepsilon}|_{x=(n-1)L_G/2} = \\ = \frac{\dot{u}|_{x=nL_G/2} - \dot{u}|_{x=-nL_G/2}}{L_G}, \quad (2)$$

where $\dot{\varepsilon}$ and $\dot{u}$ are evaluated at different positions x along the segment. We consider six cable segments and the corresponding nodes: N19–16, N18–19, N16–18, N10–11, N9–10, N3–4. Given our experimental setup (2.4 m of channel spacing and 5 m of gauge length), the left-hand side of Eq. (2) is equivalent to the summation of one DAS channel every two along each fibre segment, in order to mitigate the spatial-averaging effect of the gauge length. We obtain the components of the seismic velocity along the fibre direction by rotating the 3 components of each node according to the azimuth and slope of the corresponding cable segment. In the right-hand side of Eq. (2) we differentiate these longitudinal components to ensure an accurate comparison with DAS data.

Fig. 5 exhibits the comparison between the strain rate derived from DAS and nodes using Eq. (2) for the explosion shown in Fig. 4 and for 20 s of volcanic tremor, in both time and frequency domains. In the 2–15 Hz frequency band, DAS and node strain rate waveforms show an excellent agreement in phase. The maximum cross-correlation coefficients between DAS and node traces reach a value of 0.99 for the explosive event (Fig. 5a) and 0.98 for the volcanic tremor-only phase (Fig. 5c). Therefore, we obtain a better correlation between DAS and node data than using Eq. (1) in Section 3.

However, DAS strain rate exhibits lower amplitudes with respect to the strain rate derived from the nodes. To systematically estimate these amplitude differences in the time domain, we use the following workflow. Firstly, we apply a recursive STA/LTA al-

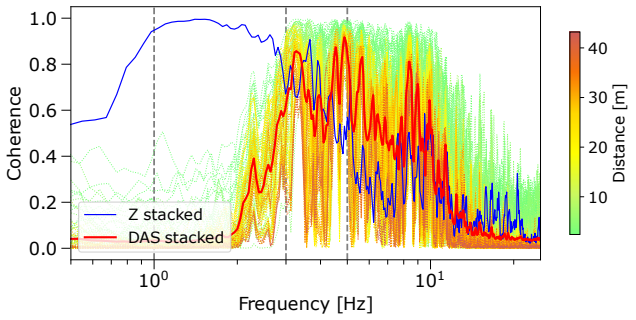

Figure 8. In red, average coherence computed during the unfiltered one-hour long strain rate time series (09/22/2020 19:34–20:34) between all of the 135 channel pairs in the 3 segments of the DAS-L array. Coherence traces of each pair are also shown as dotted lines (with colors relative to the distance between the two channels). In blue, average coherence between the N component of each node pair in the array N15–19 during the same period of time. Grey vertical dashed lines mark the values of 1, 3 and 5 Hz, that are the limits of the two frequency bands (i.e. 1–3 and 3–5 Hz) for which we compare array analysis results with strain rate and seismic velocity data.

gorithm (Beyreuther et al., 2010) over the strain rate time series. This enables us to detect 17 explosive events of varying intensity, as displayed in Fig. 6. Next, for each segment we compute the ratio R between Root Mean Square (RMS) amplitudes of nodes and DAS strain rate traces for 4-second time windows centered on each explosive event. Additionally, we perform the same calculations during volcanic tremor phases. This process is repeated for 20 separate time intervals of tremor, each lasting 20 seconds.

As seen in Fig. 6a, node to DAS amplitude ratios (R) averaged across all segments are almost identical for tremor (2.72±0.82) and explosions (2.76±0.70). Only segment N9–10 (not shown) has higher R (4.76). With this exception, the other segments tested all show values of R around between 2 and 3. Furthermore, R values do not exhibit any correlation with the distance from the active craters and neither with the magnitude of the explosions (Fig. 6a) or with the frequency (Fig. 5b,d).

5 SLOWNESS VECTOR ESTIMATION

5.1 Methodology

After validating the DAS strain rate, we investigate whether it could provide meaningful information about the location of the volcanic sources. To do so, we estimate the slowness vector using strain rate records and compare the outcomes with those obtained using co-located nodes. Slowness vector estimation provides information about the apparent velocity and the back-azimuth of incoming waves. Therefore, it is a valuable tool for locating signals generated by the Strombolian activity and for wavefield characterisation (Chouet, 1996). The characteristics of seismo-volcanic signals such as explosion and tremor (e.g., the emergent onset and the absence of body wave phases) make it necessary to use array processing techniques for locating them (Chouet, 1996; Métaxian et al., 2002; Wassermann, 2012; Inza et al., 2014).

In this study, we apply the array analysis technique of Métaxian et al. (2002), which is particularly suited for volcanic tremor sources and small-aperture arrays with respect to the wavelength. Métaxian et al. (2002) demonstrated the accuracy of this method for recovering the slowness vector of volcanic sources using arrays with apertures lower than 70 m for frequencies between 0.5–5 Hz and wavelengths approximately between 160–800 m. The method consists of slowness vector estimation by inversion of the time delays between each pair of sensors i and j in a network. Time delays are estimated with the cross-spectral method (e.g., Poupinet et al. 1984) on subsequent sliding time windows. The computed time delays have a precision below half the sampling rate (Métaxian et al., 2002). Moreover, the method is independent of the amplitude of the signals, which is favourable in our case as strain rate data show significant amplitude variations along the cable. Furthermore, the amplitudes of the strain rate signals recorded by DAS are lower than those obtained with nodes.

Under the hypothesis of a unique dominant incoming plane wave the expected theoretical delays τ are given by the equation:

$$\tau_{ij} = \mathbf{s} \cdot \mathbf{r}_{ij}, \tag{3}$$

where the dot denotes the usual scalar product, $\mathbf{s} = (-||s|| \sin\theta, -||s|| \cos\theta)$ is the slowness vector, θ is the back-azimuth, measured clockwise from the north and $\mathbf{r}_{ij}$ is the relative position vector between stations pairs. Given a set of measured time delays τ_{ij}, with respective errors $\sigma_{\tau_{ij}}$, estimated for each time window, the two components of the slowness vector $\mathbf{s}$ are calculated by linear inversion of the N(N-1)/2 equations (3), where N is the number of sensors in the array. The problem is over determined for N≥3 and can be solved by standard least squares method.

5.2 Data selection

We select seismic velocity and strain rate records during the one-hour long time series between 19:34–20:34 on 09/22/2020. Hereafter we describe the selected array geometries and data, first for the nodal and then for the DAS arrays.

The nodal array we consider is composed of nodes N15–19 (Fig. 7a) forming a triangle in the upper part of the network (Fig. 1d). The seismic antenna has an aperture of 53 m and a minimum inter-receiver distance of 15 m. These dimensions allow us to observe time delays for waves with wavelengths of a few hundred metres. The array response function (ARF) of the N15–19 array (between 3–5 Hz) is displayed in Fig. S2c. The 5 nodes in the N15–19 array provide 10 pairs of time delay measurements computed along subsequent 16-second time windows with a 1-second shift. The window size must be long enough to obtain precise calculations of the slowness values through linear interpolation of the cross-spectrum phase (Métaxian et al., 2002). Too long windows, however, decrease the resolution of the results. We select these sliding window parameters after several tests, aiming to find a balance between the dispersion of the results and the shortest possible length. We perform the analysis in 3 frequency bands (1–3, 3–5, and 5–7 Hz) and for the 3 components of the nodes. Fig. 7d,g,l show the 16-second waveforms corresponding to an explosion (same as in Fig. 4) recorded by the 3 components of the nodal N15–19 array.

To analyse the strain rate records we select three different array geometries:

(1) the first configuration (named DAS-L) consists of 3 linear segments (Fig. 7b), each composed of 10 channels (∼ 40 m) with similar orientation (250±10°). The array has an aperture of 170 m and a minimum inter-receiver distance of 2.4 m (as all DAS arrays). The 3 segments of the DAS-L array are located at different distances from the craters, which is supposed to yield favorable results with our method.

(2) The second array (named DAS-T) has a triangular geometry,

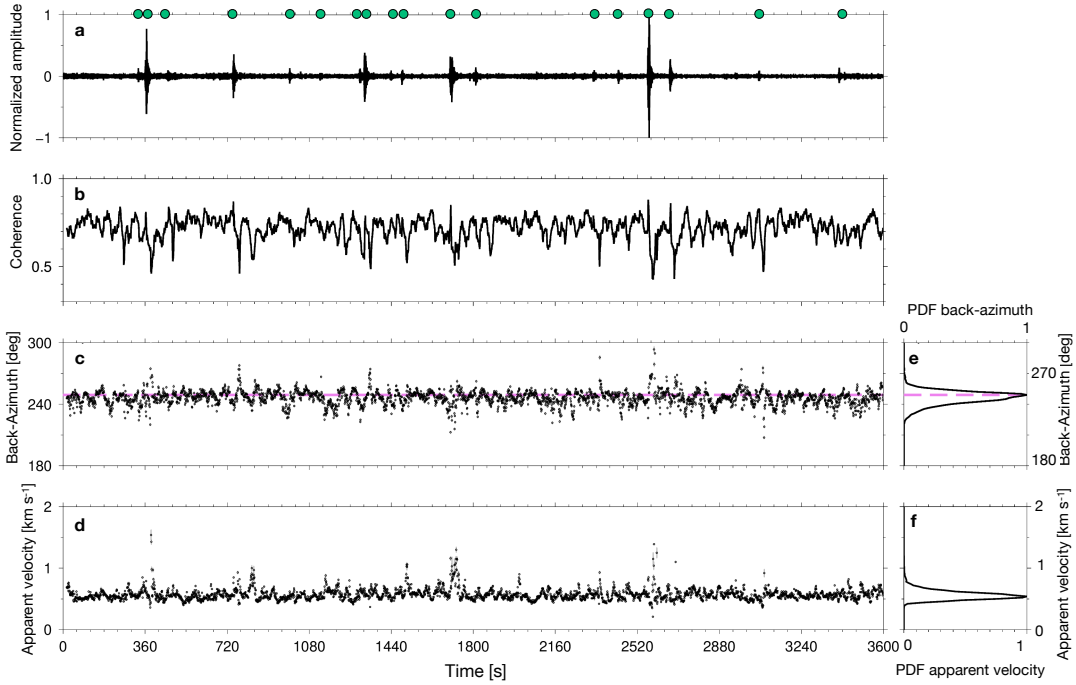

Figure 9. (a) One-hour seismic velocity trace of the N component of node N16 band-pass filtered between 3–5 Hz. Green circles in (a) mark the detected explosive events. Array processing results obtained with the nodal N15–19 array are in b-f considering one hour of signals. (b) mean coherence between traces in each time window. (c) back-azimuths and (d) apparent velocities obtained with the method described in Section 5. Corresponding PDFs are shown in (e) and (f). Pink dashed lines in (c) and (e) indicate the back-azimuth of the central point of the active craters with respect to the array centroid.

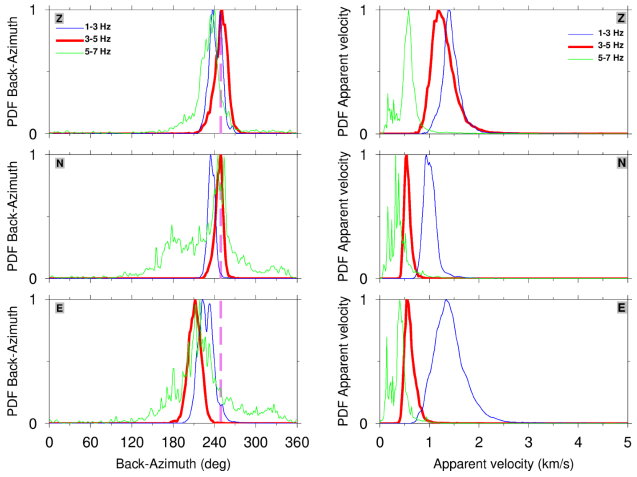

Figure 10. PDF results of back-azimuth (left column) and apparent velocity (right column) in the frequency bands of 1–3 (blue), 3–5 (red), 5–7 (green) Hz for the Z, N, and E components of the nodal array N15-19 during the analysed one-hour time series (09/22/2020 19:34–20:34 UTC). The dashed lines in the left column represent the direction of the central part of the active craters (251°).

which is expected to be more adequate than the linear layout for the slowness vector estimation (Hudson et al., 2021; Näsholm et al., 2022). It is composed of the three sides (Fig. 7c) of the triangle-shaped deployment at the end of the fibre (Fig. 1d), and has an aperture of 43 m.

(3) The third array (named DAS-TL) is a combination of the previous two (Fig. S3c). The DAS-TL array is composed of the three segment of the DAS-T array and one segment (DAS-L2 in Fig. 7b) of the DAS-L array. It has an aperture of 100 m.

To evaluate the resolution and sensitivity of the three DAS arrays, we compute the relative ARFs by taking into account the strain rate polarization patterns for P/SV/Rayleigh and SH/Love waves (Martin, 2018; Zhan, 2019; Trabattoni et al., 2022). The radiation patterns for seismic velocity and strain rate are similar for P/SV/Rayleigh waves (Fig. S3g), whereas they are different for SH/Love waves (Fig. S3m). We consider synthetic plane waves with a frequency of 5 Hz and a velocity of 500 m/s coming from the direction of the active craters (250°) in Fig. S3 and from an orthogonal back-azimuth (160°) in Fig. S4. For both P/SV/Rayleigh and SH/Love waves, all three array configurations exhibit correct slowness estimates for the given wave source and all wave types (Figs. S3 and S4). The DAS-L array provides lower resolution in the slowness direction perpendicular to the cable (Figs. S3h, S4h) and, as expected, triangle-shaped geometries exhibit more isotropic ARFs (Näsholm et al., 2022). Additionally, the DAS-TL array shows sharper main peak due to its larger aperture. Taking into account the wave polarization does not change much the ARFs for P/SV/Rayleigh waves but it increases the ARF resolution for SH/Love waves. These results show that the selected array configurations are well suited for recovering the slowness vector. Furthermore, our inversion method provides more accurate results than conventional beamforming (Métaxian et al., 2002).

The first step in our method (Section 5.1) is to measure differential travel times. Because the cross-spectral method for the time delay estimation strongly relies on the coherence between traces recorded across the array, we investigate the variation with distance and frequency of the similarity between strain rate waveforms. To this aim, we calculate the average coherence between all pairs of

Table 1. Maximum values and confidence intervals of the PDFs of both back-azimuth and apparent velocity computed during one hour of data for Z, N, and E components of the nodal array (N15–19). The craters' back-azimuth with respect to the centroid of the nodal array ranges between 246-256°.

Component	Parameter	Frequency band		
		1–3 Hz	**3–5 Hz**	**5–7 Hz**
Z	Back-azimuth [°]	238 ± 10	251 ± 10	240 ± 11
	Apparent velocity [km/s]	1.40 ± 0.14	1.18 ± 0.26	0.58 ± 0.10
N	Back-azimuth [°]	234 ± 8	248 ± 8	245 ± 6
	Apparent velocity [km/s]	0.94 ± 0.18	0.54 ± 0.06	0.32 ± 0.04
E	Back-azimuth [°]	222 ± 14	212 ± 10	219 ± 5
	Apparent velocity [km/s]	1.34 ± 0.32	0.54 ± 0.10	0.40 ± 0.10

DAS channels in the DAS-L array during the one-hour time series. For comparison, we do the same for the sensors composing the nodal array (N component). Fig. 8 compares the coherence between DAS channels with coherence between nodes. We observe that the coherence is maximum below 3 Hz for the nodes, while it is maximum between 3 and 5 Hz for the DAS. The lack of high resolution below 3 Hz for the DAS can be explained by its high noise levels (Fig. 3). Additionally, Fig. 8 shows that the coherence between DAS channels rapidly decreases with increasing channel distance, even within a range below 40 m. Therefore, we estimate the time differences separately for each segment of the DAS arrays. Having 10 channels for each segment, we obtain 45 time delays. This gives 135 equations like Eq. (3) for the DAS-L and DAS-T arrays and 180 for the DAS-TL array. For each array configuration, we retrieve the slowness vector by inverting the corresponding time delays.

For the slowness vector calculation with strain rate data, we use 16-second windows with 1-second shifts and focus on two frequency bands, i.e. 1–3 and 3–5 Hz. Data filtered between 3–5 Hz are shown in Fig. 7 for one explosion. We observe a high similarity between strain rate waveforms of each cable segment, which is required for high resolution differential travel time measurements.

5.3 Slowness vector estimation with the nodal array

We apply the method described in Section 5.1 to determine back-azimuth and apparent velocity with seismic velocity data. Fig. 9c,d show that these parameters, estimated for each window between 3–5 Hz for the N component of the nodal array, are stable during the entire hour for the background volcanic tremor. On the other hand, in the explosion coda, the decrease in coherence (Fig. 9b) gives less accurate time delays and consequently higher variability of the inverted back-azimuth and apparent velocity (Fig. 9c,d). Probability density functions (PDFs) are shown in Fig. 9e,f. The back-azimuth PDF is maximum at 251°, i.e. pointing towards the central part of the crater area that ranges between 246–256°. The corresponding apparent velocity PDF is maximum at 0.54 km/s. Considering a wider array with an aperture of 105 m (Fig. S2) gives similar slowness vector (Fig. S5).

Fig. 10 summarizes the back-azimuth and apparent velocity PDFs obtained for each component and frequency band during the considered time frame. Table 1 exhibits the maximum PDF values and their confidence intervals. Back-azimuth PDFs between 3-5 Hz have narrower peaks than in the other frequencies and appear better resolved: the obtained values point towards active craters (246–256°) when considering the Z (251°) and N (248°) components, while the E component exhibits a southward shift of ∼20-30°. These results show that the apparent velocities are frequency-dependent, especially for the horizontal components. It may be due to dispersive waves or to the fact that at different frequencies, different phases dominate.

5.4 Slowness vector estimation with DAS arrays

We now estimate the slowness vector from the DAS strain rate data of the three arrays selected in Section 5.2. We then compare the results with those obtained from the nodal N15–19 array in Section 5.3. Fig. 11 shows higher variability with time of the results obtained with DAS-L and DAS-T arrays compared to the nodal array (N component), but similar PDF maxima.

Back-azimuth PDF (Fig. 11h) for the DAS-L array is centred at 256°, i.e., towards the crater direction (246-256°). Back azimuth PDF for the DAS-T array (Fig. 11h) exhibit instead a ∼10° southward shift. These results are consistent with waves propagating from the volcano summit area, ∼200 m away from the active crater area. Apparent velocities obtained from the strain rate and seismic velocity (N component) measurements are similar, i.e. ∼0.67 and ∼0.54 km/s, respectively (Fig. 11i). Fig. 12 shows that the slowness vector estimates obtained with the N component of the nodal array and with the three DAS arrays between 3–5 Hz are in agreement.

Table 2 summarizes both back-azimuth and apparent velocity PDF maxima and confidence intervals between 1–3 and 3–5 Hz for the three DAS configurations. In both frequency bands, The back-azimuth results of the DAS-L array exhibit a wider distribution than the other two, as marked by higher standard deviations (Table 2). This is probably due to the lower broadside resolution of the linear geometry (Figs. S3 and S4). We observe almost identical back-azimuths obtained with the DAS-T and DAS-TL arrays in the two frequency bands. For all DAS geometries, apparent velocities are comparable in the two frequency bands and range between 0.58–0.68 km/s.

6 DISCUSSION

We recorded strain rate signals generated by ordinary Strombolian activity. We observe a persistent background volcanic tremor and several explosive events of varying intensity in the data. Nevertheless, the instrumental noise floor prevents the recovery of most signals outside the 2–15 Hz range. Within this range, the strain rate sensed by DAS shows a perfect agreement in phase with the strain rate estimated from the nodes along 6 cable segments.

However, DAS strain rate amplitudes are more than two times lower than nodes. Despite retrieving small differences in amplitude

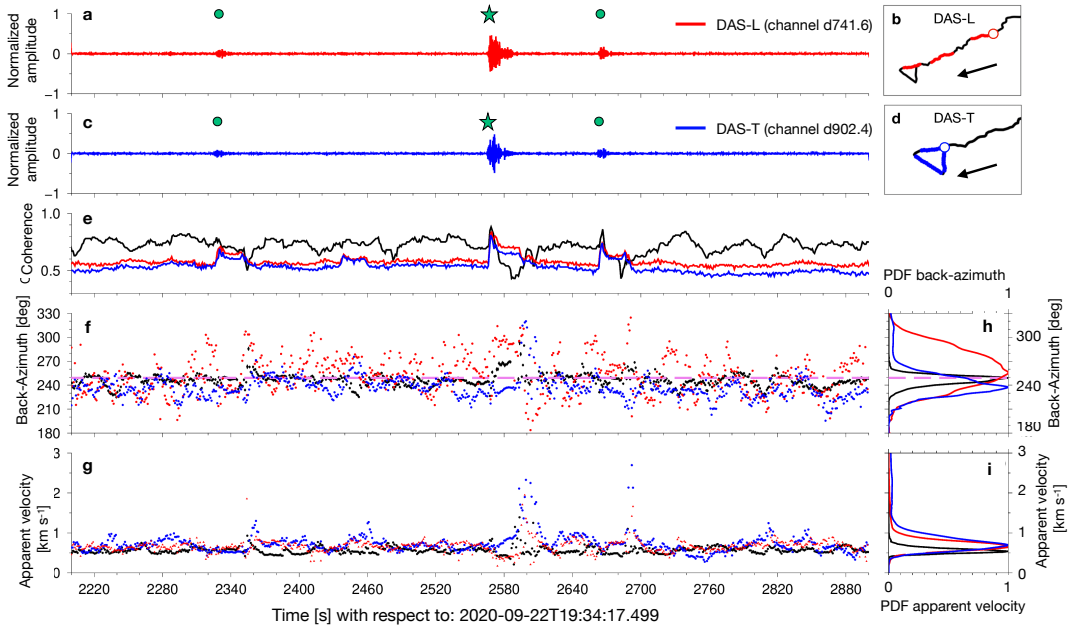

Figure 11. Strain rate traces corresponding to channels (a) d741.6 (in red) and (c) d902.4 (in blue) arrays, normalized and band-pass filtered between 3–5 Hz. Green circles in (a) and (c) mark the detected explosive events, while the green star marks the most intense event during the time period considered. (b) and (d) show the geometries of the DAS-L and DAS-T arrays. White circles in (b) and (d) mark the location of channels d741.6 and d902.4 along the cable. Black arrows in (b) and (d) represent the back-azimuth of the central part of the crater area (251°) with respect to the array centroids. Array processing results are in e-i for the DAS-L (red) and DAS-T (blue) arrays and for the N component of the nodal N15–19 array (black). (e) mean coherence between traces in each time window. (c) back-azimuths and (d) apparent velocities obtained with the method described in Section 5.1. Corresponding PDFs are shown in (h) and (i). Dashed lines in (f) and (h) indicate the direction of the active craters.

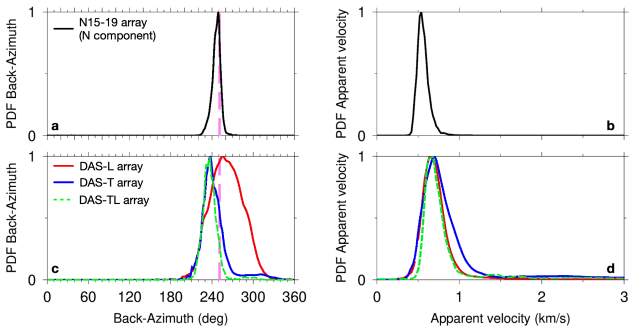

Figure 12. PDFs of back-azimuth (left column) and apparent velocity (right column) in the 3–5 Hz frequency band for the N component of the nodal N15-19 array (top row, in black) and for the DAS-L (red), the DAS-T (blue), and the DAS-TL (green) arrays (bottom row). The dashed lines in the left column represent the direction of the central part of the active craters (251°).

between DAS and node strain rate, Wang et al. (2018) and Jousset et al. (2022) do not obtain this significant gap after applying the same finite-difference relationship. Additionally, the strain changes derived from a seismic array at Etna volcano by Currenti et al. (2021) closely match the DAS measurements, even in amplitude. We suppose that the lower amplitudes of the DAS strain rate record can be due to ground-to-fibre coupling effects or, more likely, to the response to a deformation of the loose fibre bundle inside the cable (see Supplementary Note A in Supplementary Information). Her & Huang (2011), Reinsch et al. (2017), and Diaz-Meza et al. (2023) point out that the cable structure can significantly influence the ground-to-fibre strain transfer and, therefore, the amplitude of the recorded dynamic strain rate signals.

The amplitudes of the strain rate signals show marked variability along the fibre path. In particular, DAS measurements reveal an area between channels d662.4–d751.2 characterised by strain rate signal amplitudes up to 10 times greater than those found in other fibre sectors (Fig. 4d). This amplitude contrast correlates quite precisely with a change in topography along the slope observed in Figs. 1 and S1. Fig 4c,d show slower wave velocities where higher strain rate amplitudes are present. We suggest that this variation in topography along the slope underlies a change in the waves velocity. The velocity contrast would lead to different site effects that strain rate measurements are notably responsive to (Trabattoni et al., 2022). As inferred from Eq. (1) and pointed out by Lior et al. (2021) and Trabattoni et al. (2022), slower waves result in higher strain rate values recorded by the DAS. Furthermore, Trabattoni et al. (2022) point out that the wavelength decrease of a wave entering a low-velocity layer influences DAS recordings twice as much as in the case of seismic velocity measurements.

The slowness vector provides information on the eruptive source location. However, with our method, we can only conclude on trends of the dominant components of the wavefield which is a mixture of body and surface waves on volcanoes (Chouet et al., 1997; Métaxian et al., 1997; Saccorotti et al., 2001; Konstantinou & Schlindwein, 2003). The application of this methodology to strain rate data requires some adaptations compared to its typical use with inertial sensors. First, DAS data exhibit a direction-dependent sensitivity, described by, e.g., van den Ende & Ampuero (2021), Klaasen et al. (2021), Näsholm et al. (2022). Furthermore, the strain rate is measured parallel to the topography. As implied

Table 2. Maximum values and confidence intervals of the PDFs of both back-azimuth and apparent velocity computed during one hour of data for the DAS-L, DAS-T, and DAS-TL configurations. The craters' back-azimuth with respect to the centroid of the three arrays ranges between 246-256°.

Component	Parameter	Frequency band	
		1–3 Hz	3–5 Hz
DAS-L	Back-azimuth [°]	267 ± 32	256 ± 18
	Apparent velocity [km/s]	0.68 ± 0.15	0.66 ± 0.08
DAS-T	Back-azimuth [°]	222 ± 12	237 ± 11
	Apparent velocity [km/s]	0.58 ± 0.14	0.68 ± 0.14
DAS-TL	Back-azimuth [°]	220 ± 9	238 ± 12
	Apparent velocity [km/s]	0.68 ± 0.2	0.68 ± 0.14

by Eq. (1), and stated by van den Ende & Ampuero (2021), sub-horizontal waves are favoured by DAS measurements over waves with fast apparent velocities (e.g., reaching the array with steep inclination).

At Stromboli, the 1–10 Hz tremor and explosive sources are located at the same altitude as the fibre network (Chouet et al., 1997; Ripepe et al., 2021a). Therefore, we mainly record surface or body waves propagating sub-parallel to the optical fibre, which is a favourable condition for DAS measurements. This feature allows us to obtain accurate slowness vectors with strain rate data.

We validate the results obtained with strain rate measurements using the array of co-located nodes between 1–3 and 3–5 Hz. Between 1–3 Hz, back-azimuths derived from the nodes are 10 to 30° south of the active craters, whereas, for the DAS strain rate, back-azimuths are 10° north (DAS-L array) and 20 to 30° south (DAS-T and -TL arrays) of the active craters. A possible explanation for the observed shift in back-azimuth values obtained with both seismic velocity and strain rate data could be the fact that at these frequencies (and wavelengths) the effect of the near-field term may blur the propagative phase of the far-field term. Furthermore, the lower resolution of the selected arrays at these frequencies may adversely affect the results obtained.

In the same frequency band, apparent velocities obtained with the nodal array range between 0.94–1.40 km/s. Conversely, strain rate records also provide lower apparent velocities (0.58–0.68 km/s) than the nodes. Literature results help us interpret the apparent velocities in more detail. Chouet et al. (1997) and Wassermann et al. (2022) respectively applied polarisation analyses on 3C and six-degree-of-freedom (i.e., translational and rotational) measurements at Stromboli. They exhibited the prevalence of S-type motions between 1–3 Hz. The apparent velocities retrieved with the nodal array suggest a domination of body waves in this frequency band. Lior et al. (2021) and Trabattoni et al. (2022) instead pointed out the higher sensitivity of DAS to slower waves, which may explain the velocity discrepancy between node and DAS. Additionally, the low coherence of the strain rate record below $\sim$2 Hz (Fig. 8) may hinder a proper slowness vector estimation in this frequency band.

Between 3–5 Hz, the results of the slowness vector estimation from strain rate and seismic velocity data are in agreement, as shown in Fig. 12. Back-azimuths derived from the N and Z components of the nodal array and from the DAS-L array point towards the craters, whereas DAS-T and DAS-TL arrays point 10° further south of the crater area (Fig. 12a,c). This is however still consistent with a propagation of waves from the summit zone of the volcano and close ($\sim$200 m) to the active crater area.

We interpret the low apparent velocities obtained with the horizontal nodes and DAS arrays (around 0.60 km/s; Fig. 12b,d) as due to a prevalence of surface waves in this frequencies band. This interpretation is in agreement with Chouet et al. (1997) and Chouet et al. (1998), who suggested that the volcanic tremor at Stromboli is composed of 70% Love waves and 30% Rayleigh waves above 2.5 Hz. The authors also showed that phase velocities of Rayleigh and Love waves between 3–5 Hz at Stromboli range between 0.65–0.40 km/s and 0.65–0.55 km/s, respectively, which is in agreement with our values around 0.60 km/s. The higher velocity observed from the vertical node components (1.18 km/s) may mostly correspond to body waves.

7 CONCLUSION

In September 2020, we installed and interrogated a 1-km-long fibre-optic cable at Stromboli volcano to test DAS capabilities for active volcano monitoring. We aim to confirm two issues: (i) whether DAS accurately records seismic signals generated by Strombolian activity and (ii) whether it can reliably provide its source location. We analyse the entire dataset and show the results for an hour-long time series between 19:34–20:34 on 09/22/2020.

Firstly, we conduct a quality and calibration assessment of DAS measurements. The comparison between strain rate data sensed by DAS along 6 cable segments and derived from co-located nodes shows an excellent phase resemblance of the waveforms (average cross-correlation coefficients above 0.9). However, amplitudes recorded with DAS are, on average, $\sim$2.7 times smaller than those associated with nodes. We demonstrate that this difference can be explained by an ineffective cable-to-fibre strain transfer due to a loose cable structure (e.g., Currenti et al., 2023; Diaz-Meza et al., 2023), which we quantified.

We apply the array processing technique of Métaxian et al. (2002) to estimate the slowness vector. Results obtained from strain rate records between 3–5 Hz indicate seismic waves propagating from the volcano summit area, i.e., corresponding to or in the proximity (maximum distance of $\sim$200 m) of the active craters. We also obtain apparent velocities of $\sim$0.60 km/s, mainly corresponding to surface waves (Chouet et al., 1997; Chouet et al., 1998). The results are stable during the analysed hour, indicating a persistent source location for the explosions and the volcanic tremor. As a confirmation, back-azimuth and apparent velocity results obtained with strain rate and seismic velocity data closely match.

We demonstrated that DAS strain rate signals enable to analyse explosive events of varying intensity and volcanic tremor during ordinary Strombolian activity. Our findings confirm the capability of DAS to measure the strain rate generated by volcanic activity with high accuracy and its potential for volcanic monitoring purposes.

ACKNOWLEDGMENTS

This study would not have been possible without the work of S. Oliva and his team in digging the trench for the fibre-optic cable. Furthermore, we would like to acknowledge the valuable help offered in the field by G. Diana, M. Masini and C. Caudron for both fibre and nodes deployment. We thank C. Jestin, G. Calbris and V. Lanticq of FEBUS Optics for their support and the two reviewers, T. Hudson and P. Jousset, for their constructive comments that

helped us improving this manuscript. DAS data were processed using the Xdas Python library (`https://github.com/xdas-dev/xdas`, DOI: `10.5281/zenodo.7573824`). Seismometers data were processed using the Obspy python library (e.g., Beyreuther et al. 2010). Processing of Differential GPS data was performed with RTKLIB software (`https://rtklib.com`). Linear interpolation of DAS channels was performed with the help of the Interparc Matlab library (`https://www.mathworks.com/matlabcentral/fileexchange/34874-interparc`, John D'Errico, 2012, MATLAB Central File Exchange). This work was financially supported by the ANR-19-CE04-0011-01 MONIDAS (Natural Hazard Monitoring using Distributed Acoustic Sensing) Project.

DATA AVAILABILITY

Data used for this manuscript are available through IPGP Research Collection at the following DOI: `https://doi.org/10.18715/IPGP.2023.lgl6bxby`.

References

Ajo-Franklin, J. B., Dou, S., Lindsey, N. J., Monga, I., Tracy, C., Robertson, M., Rodriguez Tribaldos, V., Ulrich, C., Freifeld, B., Daley, T., & Li, X., 2019. Distributed Acoustic Sensing Using Dark Fiber for Near-Surface Characterization and Broadband Seismic Event Detection, *Scientific Reports*, **9**(1), 1328.

Aki, K. & Richards, P. G., 2002. *Quantitative Seismology*, University Science Books, Sausalito, CA.

Beyreuther, M., Barsch, R., Krischer, L., Megies, T., Behr, Y., & Wassermann, J., 2010. ObsPy: A Python Toolbox for Seismology, *Seismological Research Letters*, **81**(3), 530–533.

Blackburn, E. A., Wilson, L., & Sparks, R. S. J., 1976. Mechanisms and dynamics of strombolian activity, *Journal of the Geological Society*, **132**(4), 429–440.

Braun, T. & Ripepe, M., 1993. Interaction of seismic and air waves recorded at Stromboli Volcano, *Geophysical Research Letters*, **20**(1), 65–68.

Bruno, P. P. G., Maraio, S., & Festa, G., 2017. The shallow structure of Solfatara Volcano, Italy, revealed by dense, wide-aperture seismic profiling, *Scientific Reports*, **7**(1), 17386.

Capon, J., Greenfield, R., & Kolker, R., 1967. Multidimensional maximum-likelihood processing of a large aperture seismic array, *Proceedings of the IEEE*, **55**(2), 192–211, Conference Name: Proceedings of the IEEE.

Chouet, B., Saccorotti, G., Martini, M., Dawson, P., De Luca, G., Milana, G., & Scarpa, R., 1997. Source and path effects in the wave fields of tremor and explosions at Stromboli Volcano, Italy, *Journal of Geophysical Research: Solid Earth*, **102**(B7), 15129–15150.

Chouet, B., De Luca, G., Milana, G., Dawson, P., Martini, M., & Scarpa, R., 1998. Shallow velocity structure of Stromboli volcano, Italy, derived from small-aperture array measurements of Strombolian tremor, *Bulletin of the Seismological Society of America*, **88**(3), 653–666.

Chouet, B., Dawson, P., Ohminato, T., Martini, M., Saccorotti, G., Giudicepietro, F., De Luca, G., Milana, G., & Scarpa, R., 2003. Source mechanisms of explosions at Stromboli Volcano, Italy, determined from moment-tensor inversions of very-long-period data, *Journal of Geophysical Research: Solid Earth*, **108**(B1), ESE 7–1–ESE 7–25.

Chouet, B. A., 1996. New Methods and Future Trends in Seismological Volcano Monitoring. In: Monitoring and Mitigation of Volcano Hazards., pp. pp.22–97, Springer, Berlin, Heidelberg.

Chouet, B. A. & Matoza, R. S., 2013. A multi-decadal view of seismic methods for detecting precursors of magma movement and eruption, *Journal of Volcanology and Geothermal Research*, **252**, 108–175.

Currenti, G., Jousset, P., Napoli, R., Krawczyk, C., & Weber, M., 2021. On the comparison of strain measurements from fibre optics with a dense seismometer array at Etna volcano (Italy), *Solid Earth*, **12**(4), 993–1003, Publisher: Copernicus GmbH.

Currenti, G., Allegra, M., Cannavò, F., Jousset, P., Prestifilippo, M., Napoli, R., Sciotto, M., Di Grazia, G., Privitera, E., Palazzo, S., & Krawczyk, C., 2023. Distributed dynamic strain sensing of very long period and long period events on telecom fiber-optic cables at Vulcano, Italy, *Scientific Reports*, **13**(1), 4641, Number: 1 Publisher: Nature Publishing Group.

Daley, T., Miller, D., Dodds, K., Cook, P., & Freifeld, B., 2016. Field testing of modular borehole monitoring with simultaneous distributed acoustic sensing and geophone vertical seismic profiles at Citronelle, Alabama, *Geophysical Prospecting*, **64**(5), 1318–1334.

Daley, T. M., Freifeld, B. M., Ajo-Franklin, J., Dou, S., Pevzner, R., Shulakova, V., Kashikar, S., Miller, D. E., Goetz, J., Henninges, J., & Lueth, S., 2013. Field testing of fiber-optic distributed acoustic sensing (DAS) for subsurface seismic monitoring, *The Leading Edge*, **32**(6), 699–706.

Diaz-Meza, S., Jousset, P., Currenti, G., Wollin, C., Krawczyk, C., Clarke, A., & Chalari, A., 2023. On the Comparison of Records from Standard and Engineered Fiber Optic Cables at Etna Volcano (Italy), *Sensors*, **23**(7), 3735, Number: 7 Publisher: Multidisciplinary Digital Publishing Institute.

Dou, S., Lindsey, N., Wagner, A. M., Daley, T. M., Freifeld, B., Robertson, M., Peterson, J., Ulrich, C., Martin, E. R., & Ajo-Franklin, J. B., 2017. Distributed Acoustic Sensing for Seismic Monitoring of The Near Surface: A Traffic-Noise Interferometry Case Study, *Scientific Reports*, **7**(1), 11620, Number: 1 Publisher: Nature Publishing Group.

Fang, G., Li, Y. E., Zhao, Y., & Martin, E. R., 2020. Urban Near-Surface Seismic Monitoring Using Distributed Acoustic Sensing, *Geophysical Research Letters*, **47**(6), e2019GL086115.

Glasgow, M. E., Schmandt, B., & Hansen, S. M., 2018. Upper crustal low-frequency seismicity at Mount St. Helens detected with a dense geophone array, *Journal of Volcanology and Geothermal Research*, **358**, 329–341.

Hansen, S. M. & Schmandt, B., 2015. Automated detection and location of microseismicity at Mount St. Helens with a large-N geophone array, *Geophysical Research Letters*, **42**(18), 7390–7397.

Hartog, A. H., 2017. *An Introduction to Distributed Optical Fibre Sensors*, CRC Press, Boca Raton.

Her, S.-C. & Huang, C.-Y., 2011. Effect of Coating on the Strain Transfer of Optical Fiber Sensors, *Sensors*, **11**(7), 6926–6941, Number: 7 Publisher: Molecular Diversity Preservation International.

Hudson, T. S., Baird, A. F., Kendall, J. M., Kufner, S. K., Brisbourne, A. M., Smith, A. M., Butcher, A., Chalari, A., & Clarke, A., 2021. Distributed Acoustic Sensing (DAS) for Natural Microseismicity Studies: A Case Study From Antarctica, *Journal of Geophysical Research: Solid Earth*, **126**(7), e2020JB021493.

Inza, L. A., Mars, J. I., Métaxian, J. P., O'Brien, G. S., & Macedo, O., 2011. Seismo-volcano source localization with triaxial

broad-band seismic array, *Geophysical Journal International*, **187**(1), 371–384.

Inza, L. A., Métaxian, J. P., Mars, J. I., Bean, C. J., O'Brien, G. S., Macedo, O., & Zandomeneghi, D., 2014. Analysis of dynamics of vulcanian activity of Ubinas volcano, using multicomponent seismic antennas, *Journal of Volcanology and Geothermal Research*, **270**, 35–52.

Jousset, P., Reinsch, T., Ryberg, T., Blanck, H., Clarke, A., Aghayev, R., Hersir, G. P., Henninges, J., Weber, M., & Krawczyk, C. M., 2018. Dynamic strain determination using fibre-optic cables allows imaging of seismological and structural features, *Nature Communications*, **9**(1), 2509.

Jousset, P., Currenti, G., Schwarz, B., Chalari, A., Tilmann, F., Reinsch, T., Zuccarello, L., Privitera, E., & Krawczyk, C. M., 2022. Fibre optic distributed acoustic sensing of volcanic events, *Nature Communications*, **13**(1), 1753, Number: 1 Publisher: Nature Publishing Group.

Klaasen, S., Paitz, P., Lindner, N., Dettmer, J., & Fichtner, A., 2021. Distributed Acoustic Sensing in Volcano-Glacial Environments—Mount Meager, British Columbia, *Journal of Geophysical Research: Solid Earth*, **126**(11).

Konstantinou, K. I. & Schlindwein, V., 2003. Nature, wavefield properties and source mechanism of volcanic tremor: a review, *Journal of Volcanology and Geothermal Research*, **119**(1), 161–187.

La Rocca, M., Saccorotti, G., Del Pezzo, E., & Ibanez, J., 2004. Probabilistic source location of explosion quakes at Stromboli volcano estimated with double array data, *Journal of Volcanology and Geothermal Research*, **131**(1), 123–142.

Langer, H. & Falsaperla, S., 1996. Long-term observation of volcanic tremor on Stromboli volcano (Italy): A synopsis, *pure and applied geophysics*, **147**(1), 57–82.

Leva, C., Rümpker, G., & Wölbern, I., 2022. Multi-array analysis of volcano-seismic signals at Fogo and Brava, Cape Verde, *Solid Earth*, **13**(8), 1243–1258, Publisher: Copernicus GmbH.

Lindsey, N. J., Martin, E. R., Dreger, D. S., Freifeld, B., Cole, S., James, S. R., Biondi, B. L., & Ajo-Franklin, J. B., 2017. Fiber-Optic Network Observations of Earthquake Wavefields, *Geophysical Research Letters*, **44**(23), 11,792–11,799.

Lindsey, N. J., Dawe, T. C., & Ajo-Franklin, J. B., 2019. Illuminating seafloor faults and ocean dynamics with dark fiber distributed acoustic sensing, *Science*, **366**(6469), 1103–1107, Publisher: American Association for the Advancement of Science.

Lindsey, N. J., Rademacher, H., & Ajo-Franklin, J. B., 2020. On the Broadband Instrument Response of Fiber-Optic DAS Arrays, *Journal of Geophysical Research: Solid Earth*, **125**(2).

Lior, I., Sladen, A., Rivet, D., Ampuero, J.-P., Hello, Y., Becerril, C., Martins, H. F., Lamare, P., Jestin, C., Tsagkli, S., & Markou, C., 2021. On the Detection Capabilities of Underwater Distributed Acoustic Sensing, *Journal of Geophysical Research: Solid Earth*, **126**(3).

Lu, P., Lalam, N., Badar, M., Liu, B., Chorpening, B. T., Buric, M. P., & Ohodnicki, P. R., 2019. Distributed optical fiber sensing: Review and perspective, *Applied Physics Reviews*, **6**(4), 041302, Publisher: American Institute of Physics.

Martin, E. R., 2018. *Passive Imaging and Characterization of the Subsurface with Distributed Acoustic Sensing*, PhD thesis, Department of Geophysics, Stanford Univ.

McNutt, S. R. & Roman, D. C., 2015. Chapter 59 - Volcanic Seismicity, in *The Encyclopedia of Volcanoes (Second Edition)*, pp. 1011–1034, ed. Sigurdsson, H., Academic Press, Amsterdam.

Métaxian, J.-P., Lesage, P., & Dorel, J., 1997. Permanent tremor of Masaya Volcano, Nicaragua: Wave field analysis and source location, *Journal of Geophysical Research: Solid Earth*, **102**(B10), 22529–22545.

Métaxian, J.-P., Lesage, P., & Valette, B., 2002. Locating sources of volcanic tremor and emergent events by seismic triangulation: Application to Arenal volcano, Costa Rica, *Journal of Geophysical Research: Solid Earth*, **107**(B10), ECV 10–1–ECV 10–18.

Métrich, N., Bertagnini, A., & Pistolesi, M., 2021. Paroxysms at Stromboli Volcano (Italy): Source, Genesis and Dynamics, *Frontiers in Earth Science*, **9**.

Nappi, G., 1976. Recent activity of Stromboli, *Nature*, **261**(5556), 119–120, Number: 5556 Publisher: Nature Publishing Group.

Nayak, A., Ajo-Franklin, J., & the Imperial Valley Dark Fiber Team, 2021. Distributed Acoustic Sensing Using Dark Fiber for Array Detection of Regional Earthquakes, *Seismological Research Letters*, **92**(4), 2441–2452.

Neuberg, J., Luckett, R., Ripepe, M., & Braun, T., 1994. Highlights from a seismic broadband array on Stromboli Volcano, *Geophysical Research Letters*, **21**(9), 749–752.

Nishimura, T., Emoto, K., Nakahara, H., Miura, S., Yamamoto, M., Sugimura, S., Ishikawa, A., & Kimura, T., 2021. Source location of volcanic earthquakes and subsurface characterization using fiber-optic cable and distributed acoustic sensing system, *Scientific Reports*, **11**(1), 6319, Number: 1 Publisher: Nature Publishing Group.

Näsholm, S. P., Iranpour, K., Wuestefeld, A., Dando, B. D. E., Baird, A. F., & Oye, V., 2022. Array Signal Processing on Distributed Acoustic Sensing Data: Directivity Effects in Slowness Space, *Journal of Geophysical Research: Solid Earth*, **127**(2).

Poupinet, G., Ellsworth, W. L., & Frechet, J., 1984. Monitoring velocity variations in the crust using earthquake doublets: An application to the Calaveras Fault, California, *Journal of Geophysical Research: Solid Earth*, **89**(B7), 5719–5731.

Reinsch, T., Thurley, T., & Jousset, P., 2017. On the mechanical coupling of a fiber optic cable used for distributed acoustic/vibration sensing applications—a theoretical consideration, *Measurement Science and Technology*, **28**(12), 127003, Publisher: IOP Publishing.

Ripepe, M. & Gordeev, E., 1999. Gas bubble dynamics model for shallow volcanic tremor at Stromboli, *Journal of Geophysical Research: Solid Earth*, **104**(B5), 10639–10654.

Ripepe, M., Poggi, P., Braun, T., & Gordeev, E., 1996. Infrasonic waves and volcanic tremor at Stromboli, *Geophysical Research Letters*, **23**(2), 181–184.

Ripepe, M., Donne, D. D., Harris, A., Marchetti, E., & Ulivieri, G., 2008. Dynamics of Strombolian Activity, in *The Stromboli Volcano: An Integrated Study of the 2002–2003 Eruption*, pp. 39–48, American Geophysical Union (AGU).

Ripepe, M., Delle Donne, D., Legrand, D., Valade, S., & Lacanna, G., 2021a. Magma pressure discharge induces very long period seismicity, *Scientific Reports*, **11**(1), 20065.

Ripepe, M., Lacanna, G., Pistolesi, M., Silengo, M. C., Aiuppa, A., Laiolo, M., Massimetti, F., Innocenti, L., Della Schiava, M., Bitetto, M., La Monica, F. P., Nishimura, T., Rosi, M., Mangione, D., Ricciardi, A., Genco, R., Coppola, D., Marchetti, E., & Delle Donne, D., 2021b. Ground deformation reveals the scale-invariant conduit dynamics driving explosive basaltic eruptions, *Nature Communications*, **12**(1), 1683, Number: 1 Publisher: Nature Publishing Group.

Rosi, M., Bertagnini, A., & Landi, P., 2000. Onset of the persistent activity at Stromboli Volcano (Italy), *Bulletin of Volcanology*, **62**(4), 294–300.

Rosi, M., Pistolesi, M., Bertagnini, A., Landi, P., Pompilio, M., & Di Roberto, A., 2013. Chapter 14 Stromboli volcano, Aeolian Islands (Italy): present eruptive activity and hazards, *Geological Society, London, Memoirs*, **37**(1), 473–490, Publisher: The Geological Society of London.

Saccorotti, G., Chouet, B., & Dawson, P., 2001. Wavefield properties of a shallow long-period event and tremor at Kilauea Volcano, Hawaii, *Journal of Volcanology and Geothermal Research*, **109**(1), 163–189.

Schmidt, R., 1986. Multiple emitter location and signal parameter estimation, *IEEE Transactions on Antennas and Propagation*, **34**(3), 276–280, Conference Name: IEEE Transactions on Antennas and Propagation.

Schweitzer, J., Fyen, J., Mykkeltveit, S., Gibbons, S. J., Pirli, M., Kühn, D., & Kværna, T., 2012. Seismic Arrays. In: New Manual of Seismological Observatory Practice 2 (NMSOP-2), pp. pp.1–80, Potsdam : Deutsches GeoForschungsZentrum GFZ.

Sladen, A., Rivet, D., Ampuero, J. P., De Barros, L., Hello, Y., Calbris, G., & Lamare, P., 2019. Distributed sensing of earthquakes and ocean-solid Earth interactions on seafloor telecom cables, *Nature Communications*, **10**(1), 5777, Number: 1 Publisher: Nature Publishing Group.

Spica, Z. J., Perton, M., Martin, E. R., Beroza, G. C., & Biondi, B., 2020. Urban Seismic Site Characterization by Fiber-Optic Seismology, *Journal of Geophysical Research: Solid Earth*, **125**(3).

Stutzmann, E., Schimmel, M., Patau, G., & Maggi, A., 2009. Global climate imprint on seismic noise, *Geochemistry, Geophysics, Geosystems*, **10**(11).

Takano, T., Brenguier, F., Campillo, M., Peltier, A., & Nishimura, T., 2020. Noise-based passive ballistic wave seismic monitoring on an active volcano, *Geophysical Journal International*, **220**(1), 501–507.

Trabattoni, A., Festa, G., Longo, R., Bernard, P., Plantier, G., Zollo, A., & Strollo, A., 2022. Microseismicity Monitoring and Site Characterization With Distributed Acoustic Sensing (DAS): The Case of the Irpinia Fault System (Southern Italy), *Journal of Geophysical Research: Solid Earth*, **127**(9), e2022JB024529.

van den Ende, M. P. A. & Ampuero, J.-P., 2021. Evaluating seismic beamforming capabilities of distributed acoustic sensing arrays, *Solid Earth*, **12**(4), 915–934.

Wang, H. F., Zeng, X., Miller, D. E., Fratta, D., Feigl, K. L., Thurber, C. H., & Mellors, R. J., 2018. Ground motion response to an ML 4.3 earthquake using co-located distributed acoustic sensing and seismometer arrays, *Geophysical Journal International*, **213**(3), 2020–2036.

Wassermann, J., 1997. Locating the sources of volcanic explosions and volcanic tremor at Stromboli volcano (Italy) using beam-forming on diffraction hyperboloids, *Physics of the Earth and Planetary Interiors*, **104**(1), 271–281.

Wassermann, J., 2012. Volcano seismology. In: New manual of seismological observatory practice 2 (NMSOP-2), pp. pp. 1–77, deutsches geoforschungszentrum gfz. edn.

Wassermann, J., Braun, T., Ripepe, M., Bernauer, F., Guattari, F., & Igel, H., 2022. The use of 6DOF measurement in volcano seismology – A first application to Stromboli volcano, *Journal of Volcanology and Geothermal Research*, **424**, 107499.

Williams, E. F., Fernández-Ruiz, M. R., Magalhaes, R., Vanthillo, R., Zhan, Z., González-Herráez, M., & Martins, H. F., 2019. Distributed sensing of microseisms and teleseisms with submarine dark fibers, *Nature Communications*, **10**(1), 5778, Number: 1 Publisher: Nature Publishing Group.

Zhan, Z., 2019. Distributed Acoustic Sensing Turns Fiber-Optic Cables into Sensitive Seismic Antennas, *Seismological Research Letters*, **91**(1), 1–15.